Additive Manufacturing 48 (2021) 102444

Contents lists available at ScienceDirect

Additive Manufacturing

journal homepage: www.elsevier.com/locate/addma

Research paper

Effect of a helium gas atmosphere on the mechanical properties of Ti-6Al-4V alloy built with laser powder bed fusion: A comparative study with argon gas

Hiroki Amano [a,b], Takuya Ishimoto [a,c], Ryoya Suganuma [a], Keisuke Aiba [b], Shi-Hai Sun [c,d], Ryosuke Ozasa [a,c], Takayoshi Nakano [a,c,*]

[a] Division of Materials and Manufacturing Science, Graduate School of Engineering, Osaka University, 2–1, Yamadaoka, Suita, Osaka 565-0871, Japan
[b] TAIYO NIPPON SANSO Corporation, 1–3-26, Koyama, Shinagawa-ku, Tokyo 142-8558, Japan
[c] Anisotropic Design & Additive Manufacturing Research Center, Osaka University, 2–1, Yamadaoka, Suita, Osaka 565-0871, Japan
[d] School of Materials and Engineering, Beijing Institute of Technology, Beijing 100081, People's Republic of China

ARTICLE INFO

Keywords:
Laser powder bed fusion
Helium
Atmosphere
Cooling rate
Thermal conductivity

ABSTRACT

In metal additive manufacturing, the microstructures and associated mechanical properties of metal specimens can be controlled over a wide range. Although process parameters are considered important in the fabrication of functional parts, the effect of atmospheric gas has not been comprehensively documented. In laser powder bed fusion (LPBF), gas flow is used to eliminate fumes generated by laser irradiation. Simultaneously, the gas removes heat from the laser-irradiated part, which is exposed to high temperature. In this study, we investigated the capacity of helium as an alternative to argon, which is conventionally used as the LPBF atmosphere gas. He has a higher thermal conductivity and lower gas density than Ar, which may result in enhanced heat removal from the Ti-6Al-4V alloy during fabrication. Numerical simulations suggest a greater cooling rate under He flow. Further, the material built under He flow contained finer α' martensite grains and showed improved mechanical properties compared to those fabricated under Ar flow, despite the identical laser irradiation conditions. Thus, He gas is advantageous in LPBF for fabricating products with superior mechanical performance through microstructural refinement, and this is a result of its capacity for cooling and fume generation inhibition. Therefore, this study reveals the importance of the choice of atmospheric gas because of its effects on the characteristics of metallic specimens fabricated using LPBF.

1. Introduction

Additive manufacturing (AM) is a relatively new metal processing technology for the precise fabrication of arbitrarily shaped structures [1–4]. In recent studies, laser powder bed fusion (LPBF), a common AM technology, has emerged as a technique to control not only the shapes but also the microstructures of many kinds of metallic materials. Although LPBF and electron beam powder bed fusion (EBPBF) constitute powder-bed fusion-type AM, the microstructures obtained using the two methods differ significantly owing to the differences in the cooling rates; for example, finer microstructures in Ti-6Al-4V are typically obtained via LPBF [5–7] owing to the higher cooling rate. Therefore, AM (in particular, LPBF) is a promising technique for tailoring material properties depending on the metal (alloy) species by controlling the cooling rate.

By varying the process parameters, such as the laser power and laser scanning speed, changes in the thermal gradient (G) and migration rate of the solid/liquid interface (R) are achieved [8–10]. Thus, the cooling rate represented by $G{\cdot}R$ changes. Another parameter that can be changed is the atmospheric gas used in LPBF because the selection of the gas affects the range of controllable cooling rates. In LPBF, gas flows onto the building stage to remove the fumes generated during laser irradiation. However, the introduction of gas inevitably has effects, in addition to the removal of fumes; specifically, the gas removes heat from the molten part of the metal via heat transfer.

Argon or nitrogen gas is generally used as the atmospheric gas for

* Corresponding author at: Division of Materials and Manufacturing Science, Graduate School of Engineering, Osaka University, 2–1, Yamadaoka, Suita, Osaka 565-0871, Japan.
E-mail address: nakano@mat.eng.osaka-u.ac.jp (T. Nakano).

https://doi.org/10.1016/j.addma.2021.102444
Received 11 June 2021; Received in revised form 23 September 2021; Accepted 26 October 2021
Available online 8 November 2021

LPBF. There are no significant differences in the thermal conductivities or densities between Ar and N_2 gases; the selection of the gas depends on the reactivity with the metal material used. However, the use of these gases as coolants has rarely been considered. Compared to Ar and N_2, gaseous He has approximately 1/10th of their densities and approximately ten times their thermal conductivities, enabling excellent cooling. Studies on the use of He as a flow gas have reported its effects on the penetration depth of the melt pool [11] and the building speed of metal parts [12]. However, as mentioned, reports of the use of He gas as a coolant in LPBF are scant.

Therefore, the aim of this study was to clarify the effects of He gas flow on the microstructure and mechanical properties of metal specimens compared to those obtained under Ar gas flow. Moreover, numerical simulations were conducted to estimate the cooling rate during the solidification of a melt pool subjected to Ar and He flow. Finally, the correlation between the physical properties of the gas, cooling rate in the melt pool, and microstructure and associated mechanical properties of the fabricated parts are discussed.

2. Experimental

2.1. LPBF fabrication using Ar and He gases and material characterization

A Ti-6Al-4V ELI alloy plasma atomized powder (LPW Technology, UK) was used. The particle sizes were measured using a SALD-7100 particle size analyzer (Shimadzu, Japan). The particle sizes were D_{10} = 25.2 μm, D_{50} = 35.1 μm, and D_{90} = 45.7 μm. Specimens with dimensions of 10 mm (depth) × 10 mm (length) × 10 mm (height) were manufactured using an LPBF apparatus (EOS M 290, EOS, Germany). The laser beam was focused in a circular shape and had a diameter of 100 μm [13]. An XY scan strategy was used for the fabrication. The build direction was defined as the *z*-direction, and the two laser scanning directions were the *x*- and *y*-directions. The laser power, scanning speed, layer thickness, and scan pitch were set to 350 W, 1200 mm/s, 40 μm, and 100 μm, respectively. With these specimen dimensions and scanning conditions, laser scanning for each layer was completed in 0.833 s. The atmosphere in the interior of the chamber was replaced with Ar or He gas. In both cases, the gases flowed through the flow path originally built in the device, and fabrication was performed in an atmosphere having an oxygen concentration of less than 0.1%, as monitored using an oxygen analyzer in the LPBF apparatus. The gases flowed over the building table at a blow-out pressure of 56 Pa during fabrication.

The results of the analyses presented in this paper were obtained for as-built specimens, and no post-treatment was performed. The densities of the specimens were measured using the Archimedes method. The constituent phases and microstructures were investigated by field-emission scanning electron microscopy (FE–SEM, JIB–4610F, JEOL, Japan) and electron backscatter diffraction (EBSD; NordlysMax^3, Oxford Instruments, UK). To evaluate the mechanical properties, Vickers hardness tests (HM-221, Mitutoyo, Japan) and tensile tests (AGX-50kNV, Shimadzu, Japan) were performed. For the Vickers test, a test force of 0.3 kgf and a holding time of 4 s were used. For the tensile tests, a specimen with a gage length of 3.0 mm and cross-sectional dimensions of 1.2 mm × 0.8 mm was used, and testing was performed at an initial strain rate of 1.67×10^{-4} s^{-1} at room temperature in a vacuum. The tests were conducted using three specimens. A tensile load was applied along the build direction.

Quantitative results are expressed as the mean ± standard error (SE). Statistical significance was assessed using the Student's *t*-test, and significance was set at $P < 0.05$.

2.2. Numerical calculation of the cooling rate

To analyze the cooling rate, finite element analysis was performed to simulate the heat transfer and temperature changes during LPBF. COMSOL Multiphysics® 5.5 (COMSOL Inc., USA) was used for the numerical simulation. The dimensions of the finite element model were 10 mm (width) × 10 mm (depth) × 5 mm (height). In the simulation, the laser scanned the entire 10 mm × 10 mm *xy* plane to calculate the temperature distribution inside (center) and near the edges of the model. The scanning conditions described in Section 2.1 were used in the simulation. Because the heat flux from the laser beam is generally assumed to satisfy a Gaussian distribution [14–16], the three-dimensional energy distribution is expressed as a function of radius, *r*, and depth, *z* [10,17], as shown in Eq. (1).

$$Q_0(r,z) = \frac{2\alpha P}{\pi R^2 z_0} exp\left(-\frac{2r^2}{R^2}\right) \times \left(1 - \frac{z}{z_0}\right), \quad where \quad (0 < z < z_0) \tag{1}$$

Here, α is the heat absorptivity of the laser beam on the metal powder bed and molten metal; P is the laser power; R is the radius of the beam, which was set to 50 μm [13,18]; and z_0 is the penetration depth of the laser. The powder bed was not modeled, but α was set to 85% considering the high heat absorptivity of the powder bed [15]. z_0 was determined so that the simulated melt pool shape approximately matched the melt pool shape generally observed in Ti-alloy [19]. To analyze the effect of the difference in gas species, the heat source geometry (z_0) was set to be the same for He and Ar. The temporal and spatial heat transfer is governed by Eq. (2) [20,21].

$$\rho C \frac{\partial T}{\partial t} + \nabla \bullet \boldsymbol{q} = \mathrm{Q} \tag{2}$$

Here, ρ is the material density, C is the specific heat capacity, T is the temperature, t is the time, $\boldsymbol{q}$ is the heat flux vector, and Q is the amount of heat generated per unit volume. The latent heat was considered by incorporating it into the temperature dependence of the specific heat capacity [22,23]. The heat flux arising from heat conduction is represented according to Fourier's law by Eq. (3).

$$\boldsymbol{q} = -k\nabla T \tag{3}$$

Here, k is the thermal conductivity. The boundary conditions on the outer surface of the model were set using Eq. (4).

$$-\boldsymbol{n} \bullet \boldsymbol{q} = \mathrm{q_0} = \mathrm{h(T_{ext} - T)} \tag{4}$$

Here, $\boldsymbol{n}$ is the normal vector of the surface through which heat flows, h is the heat transfer coefficient, and T_{ext} is the external temperature at which the model contacts the environment. h for the lateral surfaces was set to 10 W/(m^2·K) [24]. The material density was set to 4430 kg/m^3. The values of thermal conductivity and specific heat capacity of Ti-6Al-4 V were obtained from the study of Rai et al. [25].

In this study, Ar or He gas was used as the atmospheric and flow gases. Therefore, the heat transfer coefficient, h, between the specimen top surface (building front) and the gas phase flowing directly above it changes. To analyze h, the flow velocity of each gas was measured using an anemometer (testo 440 dP, Testo, Germany) at the center of the fabrication platform under the conditions used for actual fabrication (Section 2.1). The measurement was continued for 1 min after the flow velocity stabilized. The measured velocities for Ar and He gases were 1.71 ± 0.01 and 3.38 ± 0.01 m/s, respectively. Based on the obtained fluid velocities, h between the surface of the fabricated parts and the gas phase was calculated using Eqs. (5)–(8) [26].

$$Re = \rho u l / \mu \tag{5}$$

$$Pr = \mu C_p / \lambda \tag{6}$$

$$Nu = 0.664 Re^{1/2} Pr^{1/3} \tag{7}$$

$$Nu = hl/\lambda \tag{8}$$

Here, Re is the Reynolds number, ρ is the fluid density, u is the flow velocity, l is the length parallel to the direction of the fluid, μ is the absolute viscosity, Pr is the Prandtl number, λ is the thermal

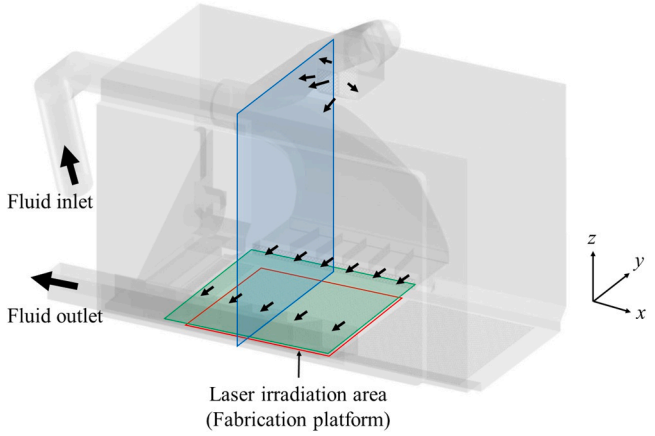

Fig. 1. Model of the LPBF apparatus used in the simulations. The red frame indicates the laser irradiation area, and the blue and green areas indicate the sections where the gas flow was observed (Fig. 2).

conductivity, C_p is the specific heat at constant pressure, and *Nu* is the Nusselt number. The respective heat transfer coefficients were calculated to be 37.9 W/(m^2·K) for Ar and 145.5 W/(m^2·K) for He gas. Under He flow, the heat transfer to the gas phase was 3.84-times greater than that under Ar flow. These heat transfer coefficient values were used for Eq. (4) for the simulation.

2.3. Simulation of gas flow and velocity

To analyze and visualize the gas flow behavior in the LPBF apparatus under the employed processing conditions, steady-state analyses based on the actual flow velocities for Ar and He gases were performed. STAR-CCM+ ® 15.02.009 R8 (Siemens, Germany) and FieldView 19 (FieldView CFD, USA) were used for the numerical simulations. The model used for the simulation is shown in Fig. 1. The simulation used the measured average flow velocity as the reference value. The steady-state analysis was solved by the finite volume method, with the continuity equations and Navier-Stokes equations shown in Eqs. (9) and (10), respectively [27].

$$\frac{\partial \rho}{\partial t} + \nabla \bullet (\rho \boldsymbol{u}) = 0 \tag{9}$$

$$\frac{\partial (\rho \boldsymbol{u})}{\partial t} + \nabla \bullet (\rho \boldsymbol{u} \otimes \boldsymbol{u}) = \nabla \bullet \boldsymbol{\sigma} + \boldsymbol{f}_b \tag{10}$$

Here, ρ is the fluid density, t is the time variable, $\boldsymbol{u}$ is the flow velocity, $\otimes$ is the Kronecker product, $\boldsymbol{f}_b$ is the force per unit volume, and $\boldsymbol{\sigma}$ is the stress tensor. This calculation enables the simulation of the stability of the gas flow at the fabrication stage, even with He, which is not typically used. Through simulation, the region of the building stage where a uniform and stable gas flow was achieved was determined for fabrication.

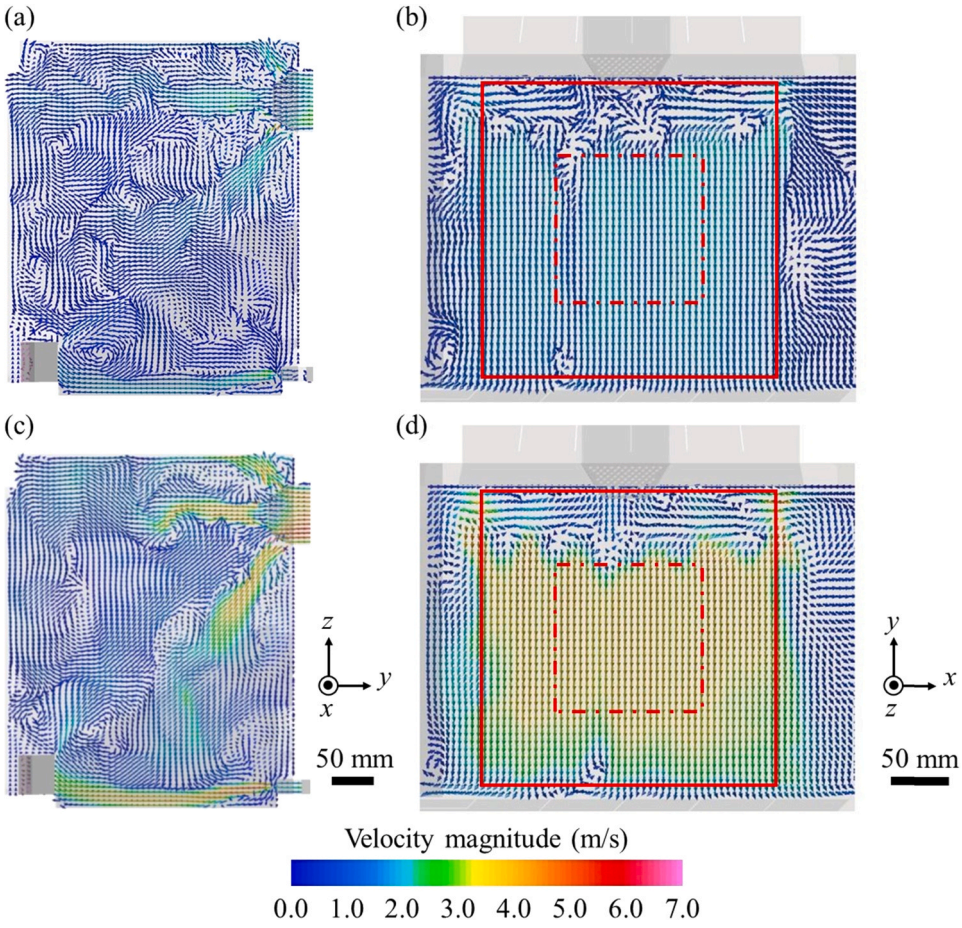

Fig. 2. Fluid flow and velocity distributions in (a, b) Ar and (c, d) He observed in the (a, c) blue and (b, d) green sections indicated in Fig. 1. The red square indicates the maximum coverage under laser irradiation, and the red dashed square indicates the area where the base plate was installed in this study (100 mm × 100 mm).

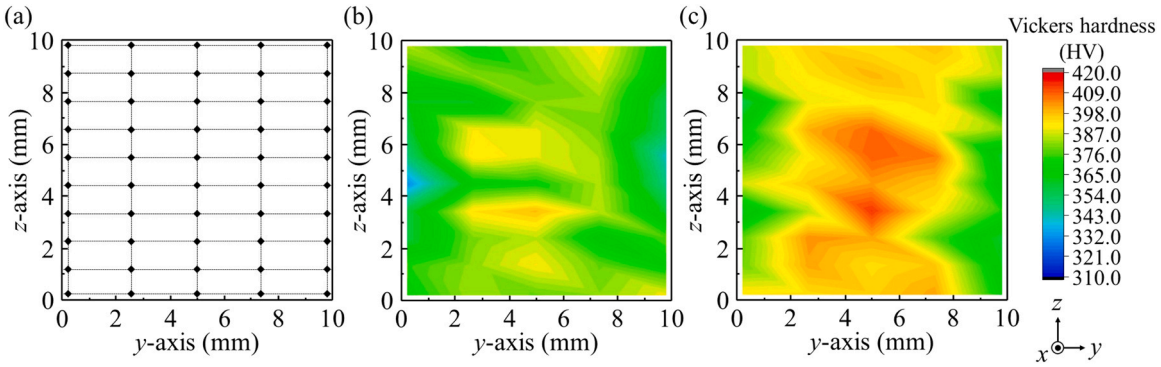

Fig. 3. (a) Schematic showing the measurement points in the *yz* plane. Distribution of Vickers hardness in the specimens fabricated under (b) Ar and (c) He flow.

3. Results

3.1. Simulation of fluid flow stability

Fig. 2 shows the fluid flow behavior and velocity distribution in the chamber simulated using the finite difference method. The flow direction and velocity of the gases were uniform over the fabrication platform (red solid squares). In this study, fabrication was performed in the central part (red dotted square) where the gas flow was more uniform to eliminate the effect of gas flow heterogeneity on the results. Movies depicting the gas flow are provided in Supplementary Movies S1(a, b).

3.2. Mechanical properties

The absolute densities of the specimens were 4.416 ± 0.001 g/cm^3 for Ar flow and 4.418 ± 0.001 g/cm^3 for He flow, and their relative densities were $99.69\% \pm 0.03\%$ and $99.72 \pm 0.04\%$, respectively. Figs. 3 and 4 show the Vickers hardness distributions analyzed in the central cross-section of the specimens fabricated using He and Ar flow, respectively. Under the flow of both gases, the hardness values at the center of the specimens tended to be higher than those at the edges. More notably, the hardness was significantly higher with He.

Fig. 5 shows the mechanical properties evaluated using tensile testing. The specimen fabricated under He flow showed an increased 0.2% proof stress and ultimate tensile strength of 4.8% and 4.5%, respectively, compared to those fabricated under Ar flow. The elongation did not change significantly.

3.3. Microstructure

Fig. 6 shows the inverse pole figure (IPF) maps and grain size (width) distributions of the specimens fabricated under each atmosphere. Almost all parts comprised acicular α' martensite grains, which are typically formed during LPBF [28], although a few β grains (less than 0.5%) were observed. The formation of the second phase is due to the very high cooling rate during LPBF; a cooling rate higher than 410 K/s is reported to induce α' transformation from the β parent phase [29]. In the center of the specimen, the median value of the grain width was smaller under He flow than under Ar flow (Fig. 6(c, e, g)). The edges of the specimens also showed a similar trend (Fig. 6(b, d, f)) to the center. The center showed a finer microstructure than the edge in both cases (Fig. 6 (h, i)).

4. Discussion

4.1. Effect of the thermal conductivity of gas on the thermal behavior in the melt pool and microstructure

The mechanical properties differed significantly depending on the gas used. The specimens fabricated under He flow exhibited superior mechanical properties. Fig. 7 shows the relationship between the grain size and Vickers hardness of each sample based on the data obtained from the center and edge of each sample, as shown in Fig. 6(a). The Vickers hardness followed the Hall–Petch relationship with $R^2 = 0.96$ and $P < 0.05$ (Fig. 7). The slope and intercept of the Hall–Petch relationship showed values similar to those reported previously [30]. The

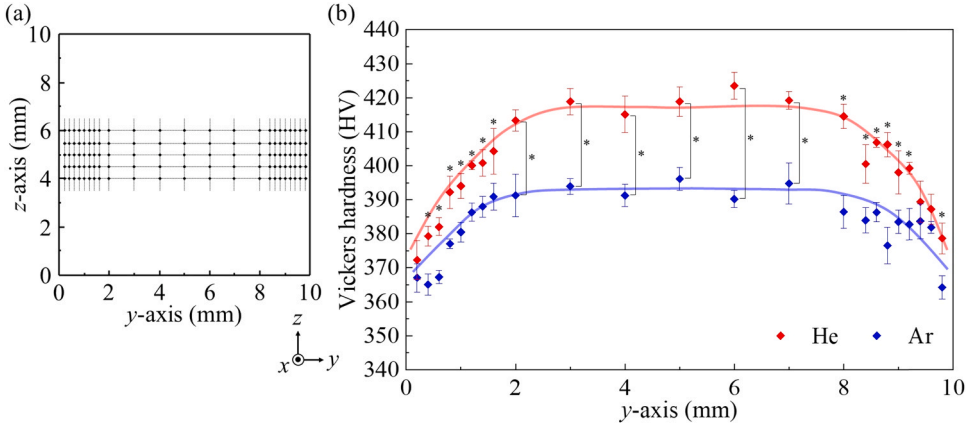

Fig. 4. (a) Schematic showing the measurement points in the *yz* plane. (b) Distribution of Vickers hardness in the specimens fabricated under Ar and He flow. * : $P < 0.05$ by Student's *t*-test.

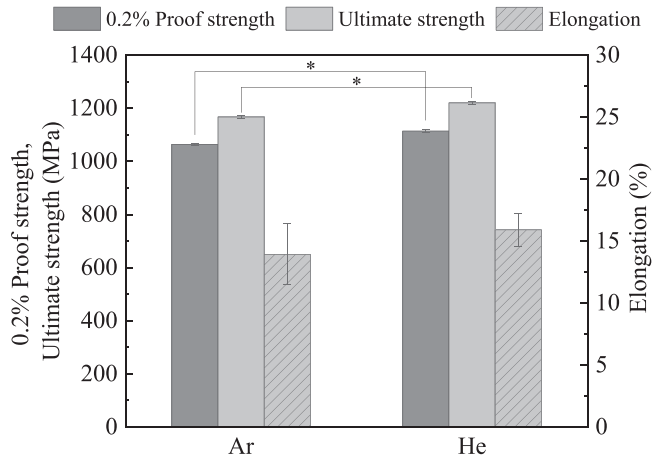

Fig. 5. Tensile properties of the specimens fabricated under Ar and He flow. * : $P < 0.05$ by Student's *t*-test.

refinement of the crystal grains achieved using He gas also resulted in superior strength.

The change in the α' martensite grain size may be due to differences in the thermal history during solidification and phase transformation. Therefore, the temperature changes under laser irradiation were calculated using numerical simulation. A heat source moving along the path shown in Fig. 8(a), which corresponds to the actual fabrication conditions, was introduced into the model, and the changes in the temperature and cooling rate induced by laser scanning were calculated. Fig. 8(b and c) show the changes in temperature at the center and edge, respectively, under Ar flow. The measurement position was set to the area with the maximum depth of the melt pool, as shown in Fig. 8(a). As shown in Fig. 8, the reciprocal scanning of the laser caused a periodic temperature increase, even after the solidification of the molten metal. However, the temperature increase was very brief, and the cyclic heating did not cause the temperature to reach the α/β transition temperature (975 °C) [31] or the martensite start (Ms) temperature of Ti-6Al-4V (800 °C) [32]. As shown in Fig. 8, the time taken for the entire solidification and cooling process at the edge of the fabricated specimen was

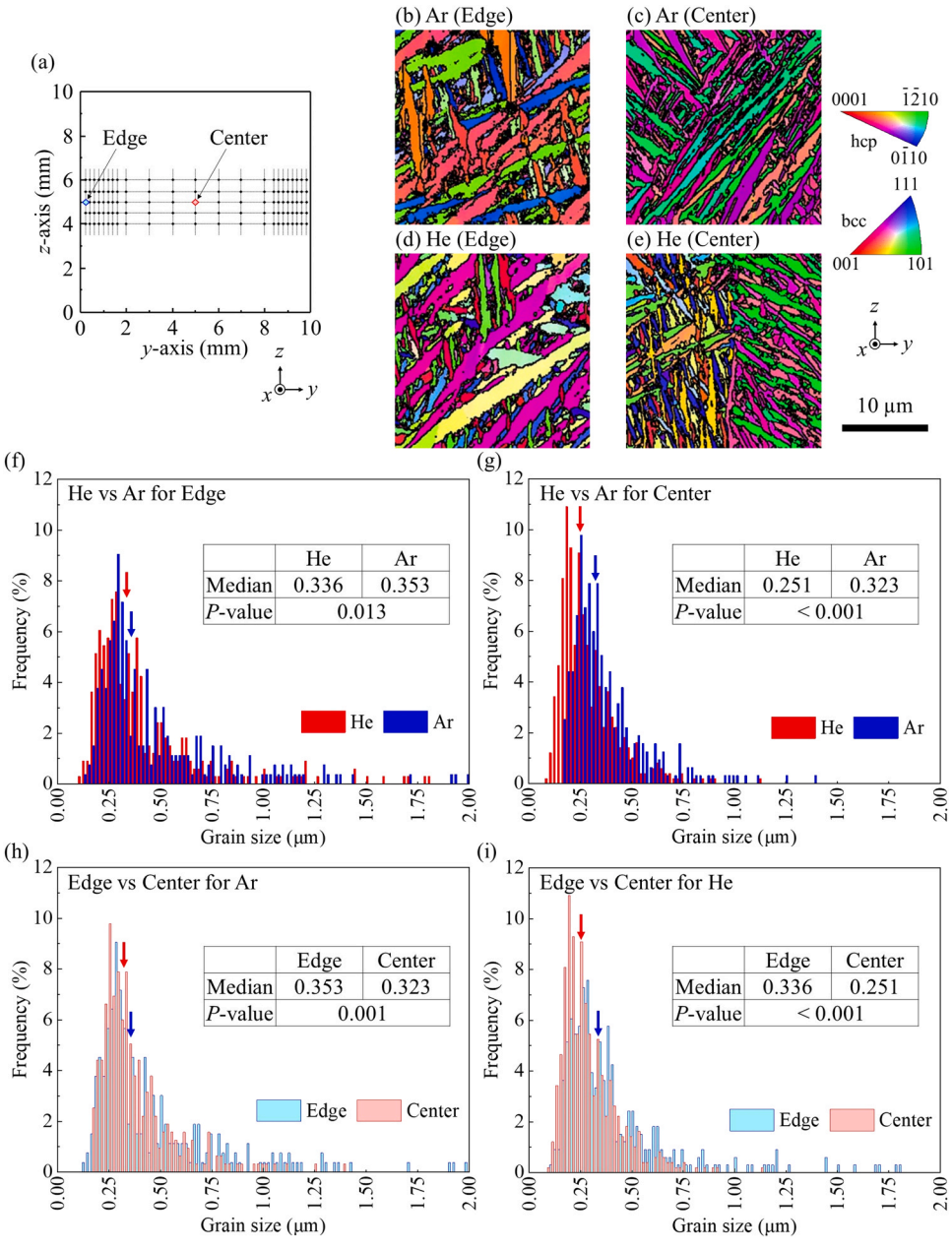

Fig. 6. (a) Schematic showing the measurement points (edge and center). Crystallographic orientation maps at (b, d) edges and (c, e) centers of the specimens fabricated under (b, c) Ar and (d, e) He flow observed along the *z*-direction. (f–i) Comparison of the distribution of the α' martensite grain sizes at the edge and center for specimens fabricated under Ar and He flow. The arrows indicate the median value of the grain size distribution. The *P*-value was determined by the Mann–Whitney *U* test.

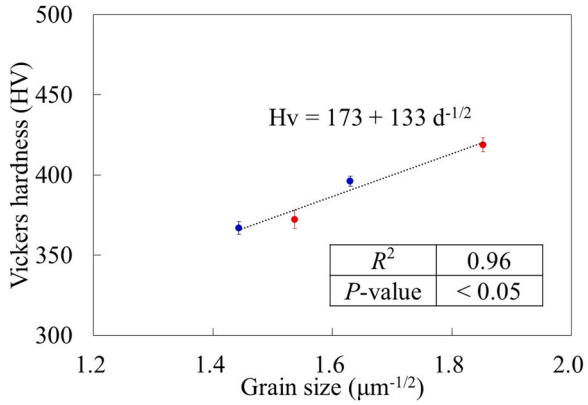

Fig. 7. Relationship between Vickers hardness and mean α' martensite grain size. Blue and red points indicate Ar and He, respectively.

approximately twice that at the center. Hence, the cooling rate during solidification differed. The cooling rate reached approximately 7×10^6 K/s immediately after the laser passed over the surface (Fig. 9). At temperatures around Ms, the cooling rate obtained by simulation was found to be higher when using He gas than when using Ar gas. In particular, the heat transfer coefficient between the specimen and gas under He flow was 3.84 times higher than that under Ar flow, suggesting that the heat dissipation from the surface of the fabricated specimens to the gas phase was accelerated. This thermal history likely caused the difference in the α' martensite grain size.

Other possible factors affecting the size of α' martensite grains are the β grain size and density of the martensite nucleation sites [33]. Smaller β grains result in finer α' martensite grains [34]. The numerical simulation indicated a higher cooling rate under He flow, suggesting smaller β grains in the specimens fabricated under He flow. However, according to the crystallographic orientation map obtained over a relatively broad region (Fig. 10), the initial β grain size was estimated to be large in both cases. The pole figures for the residual body centered cubic (bcc) β particle and hexagonal close packed (hcp) α' phase indicate that the initial β grain had a single crystalline-like strong crystallographic orientation, that is, <001> orientation in the *x*-, *y*-, and *z*-directions. This crystal orientation is consistent with the texture formed in LPBF β-Ti alloys using the XY scan strategy [19,35]. In such cases, the grain size cannot be discussed because of epitaxial growth [35]. Specifically, the α' phase that originates from the parent β grains precipitates according to the Burgers orientation relationship [36]. Therefore, the β grain size was sufficiently large in both cases and did not result in any differences in the α' grain size.

The density of α' martensite nucleation sites increases with increasing input laser energy density during LPBF, resulting in refined α' martensite grains [33]. The laser intensity reaching the specimens is significantly influenced by the spatter and fumes generated during fabrication [37–39]; significant differences in intensity can be observed even under identical laser conditions. In detail, these phenomena attenuate the intensity of the laser irradiating the specimen [37–39] but can be suppressed using He rather than Ar flow [40]; therefore, the use of He flow ensures that the laser energy is effectively delivered to the specimen being fabricated, resulting in finer α' martensite grains [33, 41–43]. In this study, the differences in laser intensity attenuation resulting from the amount of spatter and fumes generated in He and Ar flow were not considered. However, in the future, the effects of different gas species on the input and removal of heat energy into and from the melt pool will be studied comprehensively by simulation.

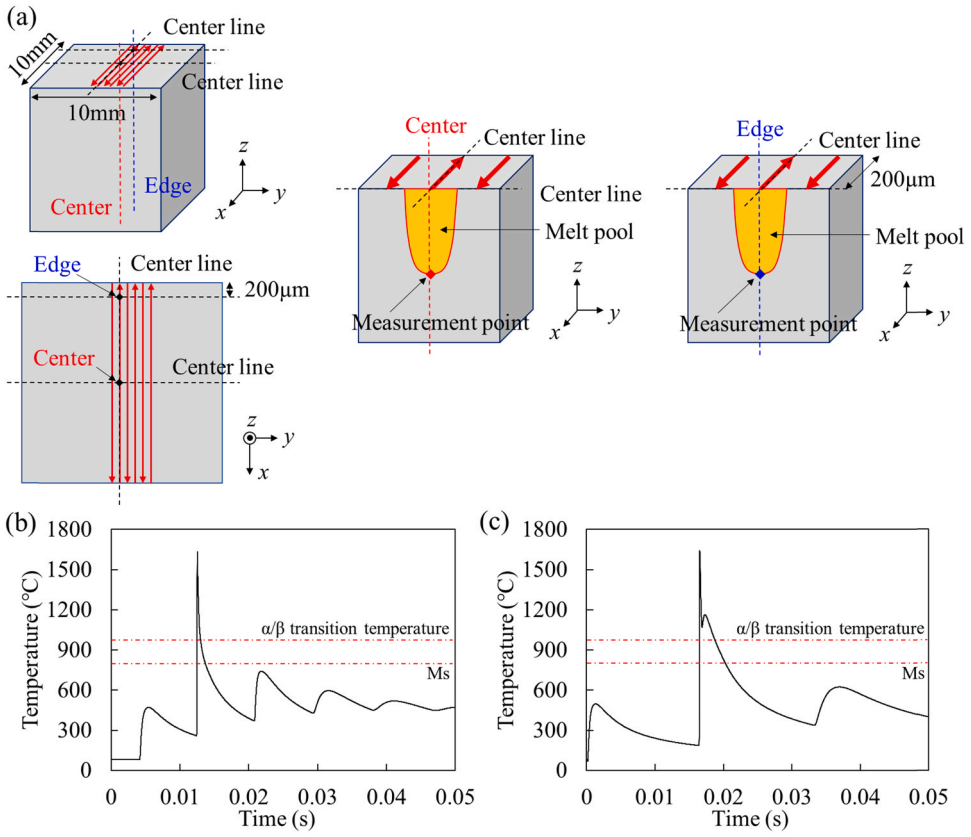

Fig. 8. (a) Schematic showing the measurement points (center and edge). Temperature changes at the (b) center and (c) edge in an Ar atmosphere. The measurement position was set to the area with the maximum depth of the melt pool.

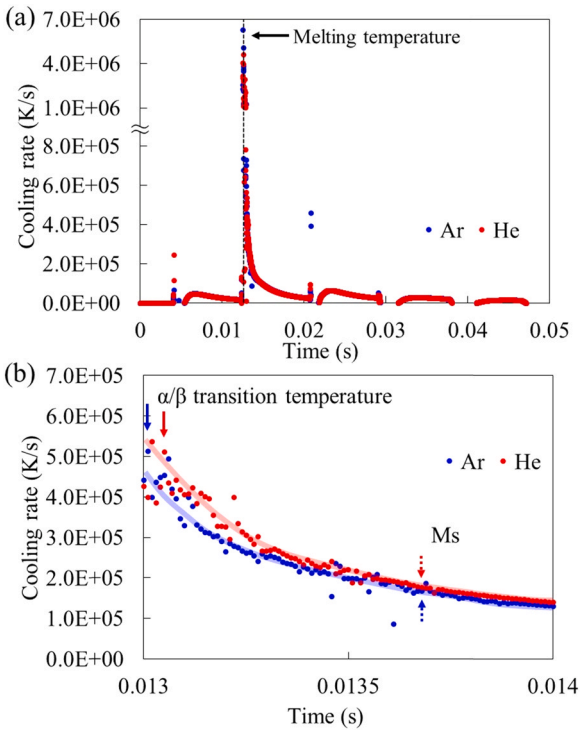

Fig. 9. (a) Variation in the cooling rates at the center of the specimens (Fig. 8 (a)) fabricated in Ar and He atmospheres. (b) Enlarged view around the temperature for α/β transformation and Ms.

4.2. Future prospects for using gas in LPBF

The results of our study indicate that, in comparison to Ar, He gas is more effective for fabricating Ti-alloy products having superior mechanical performance via LPBF through microstructural refinement because of the enhanced cooling and suppression of spatter and fume generation. Moreover, the extremely high cooling rate achieved during LPBF significantly affects the performance of metallic materials, for example, improving the corrosion resistance by suppressing the formation and growth of inclusions in 316L stainless steel [44,45], enhancing the mechanical strength by forming a supersaturated solid solution in high-entropy alloys [46], and enabling phase transformation to a non-equilibrium phase in Hastelloy X [47]. In contrast, the high cooling rate inhibits the precipitation of the strengthening phase, leading to a reduction in precipitation strengthening in tungsten [48]. We expect that these changes in the properties of metallic materials resulting from the high cooling rate of LPBF will be improved and optimized further by careful selection of the atmospheric gas species. In summary, the selection of the atmospheric gas is an important parameter for the control of microstructures and the related mechanical and chemical properties of metallic products using LPBF.

Furthermore, our findings suggest that changes in the gas flow parameters during fabrication, including non-uniformity in the direction and velocity of gas flow, have a significant effect on the microstructure and functionality of the products. In this study, the fabrication was performed within an area where the gas flow was uniform, according to the numerical simulation (Fig. 2). However, because the non-uniformity in the flow behavior, such as the variation in the flow velocity (u), becomes large near the edge of the fabrication platform, the heat transfer coefficient (h) (and therefore the cooling rate) and the resulting microstructure of the products may be dependent on the location of the part being fabricated on the platform.

Therefore, the atmospheric gas can have a significant impact on the LPBF process, which has rarely been discussed previously, and has the potential to improve product quality by careful selection. However, He gas is a non-renewable gas extracted from natural gas and is a scarce resource. Consequently, the reuse of He is essential for its application in LPBF. In addition, the use of He poses the problem of gas contamination during atmospheric circulation during LPBF fabrication [49] and gas

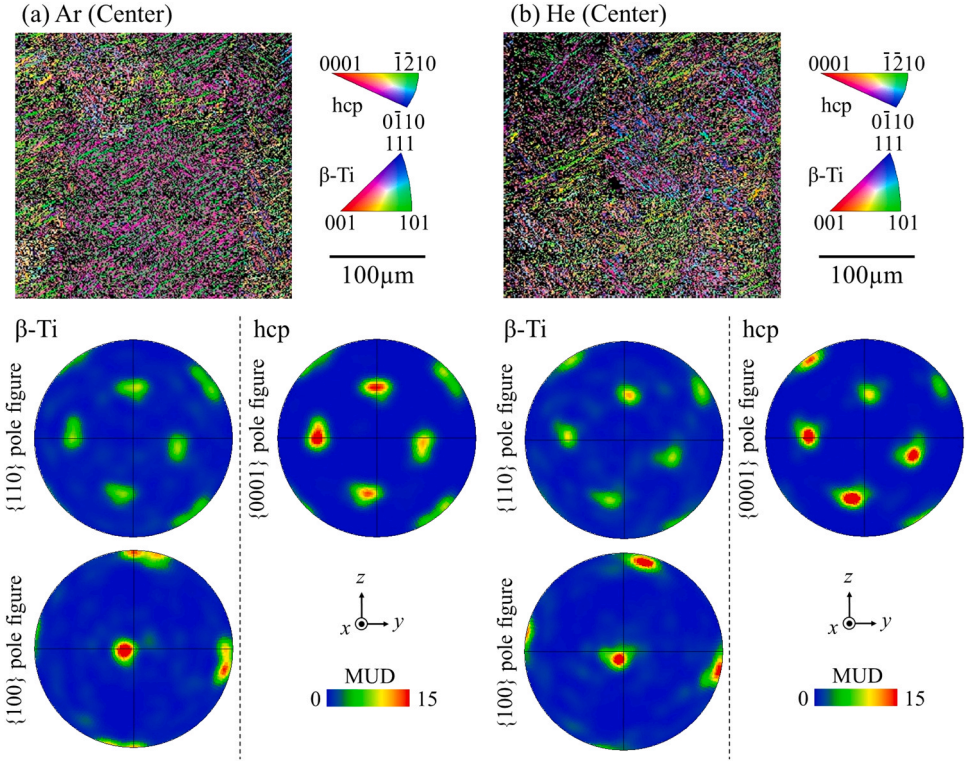

Fig. 10. IPF maps and pole figures at the center (Fig. 6(a)) of the specimens fabricated under (a) Ar and (b) He flow observed along the z-direction.

leakage from the LPBF apparatus. However, the development of He purification and recycling technologies is underway [50,51]; thus, the application of He in LPBF could be realized in the future by applying these technologies, as well as by improving LPBF equipment (e.g., improving the airtightness).

5. Conclusions

LPBF fabrication of Ti-6Al-4V under He flow, as well as conventional Ar flow, was conducted to clarify the effects of the fabrication atmosphere on the microstructures and mechanical properties of the fabricated products. Numerical simulations were performed to discuss the different effects of gas from the viewpoint of the cooling capacity of the gases used. The conclusions are as follows:

(1) Using finite volume method simulations, it was found that the gas flow over the fabrication table was unidirectional and homogeneous, and a faster velocity was observed in He than in Ar.
(2) When using He gas, the microstructure of the metal was mainly composed of α' martensite and was more refined compared to that obtained using Ar gas, resulting in significantly improved mechanical properties such as Vickers hardness, 0.2% proof stress, and ultimate tensile strength.
(3) The use of He resulted in a higher cooling rate, which led to the formation of fine α' martensite particles.
(4) The atmospheric gas used in the LPBF is an important factor affecting the microstructures and mechanical properties of metallic products.

CRediT authorship contribution statement

Hiroki Amano: Investigation, Data curation, Validation, Visualization, Writing -original draft. **Takuya Ishimoto:** Investigation, Methodology, Writing - review & editing. **Ryoya Suganuma:** Analysis, Investigation, Methodology, Visualization. **Keisuke Aiba:** Investigation, Methodology, Visualization. **Shi-Hai Sun:** Investigation, Methodology. **Ryosuke Ozasa:** Investigation, Analysis. **Takayoshi Nakano:** Conceptualization, Project administration, Supervision, Writing - review & editing.

Funding

It was supported by Grants-in-Aid for Scientific Research from the Japan Society for the Promotion of Science (JSPS) [grant number JP18H05254], and also partly supported by the Cross-Ministerial Strategic Innovation Promotion Program (SIP) – Materials Integration for Revolutionary Design System of Structural Materials –Domain C1: "Development of Additive Manufacturing Process for Ni-based Alloy" from the Japan Science and Technology Agency (JST).

Declaration of Competing Interest

The authors declare that they have no known competing financial interests or personal relationships that could have appeared to influence the work reported in this paper.

Appendix A. Supporting information

Supplementary material related to this article can be found online at doi:10.1016/j.addma.2021.102444.

References

[1] N. Aage, E. Andreassen, B.S. Lazarov, O. Sigmund, Giga-voxel computational morphogenesis for structural design, Nature 550 (2017) 84–86, https://doi.org/10.1038/nature23911.
[2] J.-H. Zhu, W.-H. Zhang, L. Xia, Topology optimization in aircraft and aerospace structures design, Arch. Comput. Methods Eng. 23 (2016) 595–622, https://doi.org/10.1007/s11831-015-9151-2.
[3] S. Liu, Y.C. Shin, Additive manufacturing of Ti6Al4V alloy: A review, Mater. Des. 164 (2019), 107552, https://doi.org/10.1016/j.matdes.2018.107552.
[4] P. Wang, J. Song, M.L.S. Nai, J. Wei, Experimental analysis of additively manufactured component and design guidelines for lightweight structures: A case study using electron beam melting, Addit. Manuf. 33 (2020), 101088, https://doi.org/10.1016/j.addma.2020.101088.
[5] H. Gong, K. Rafi, H. Gu, G.D.J. Ram, T. Starr, B. Stucker, Influence of defects on mechanical properties of Ti–6Al–4V components produced by selective laser melting and electron beam melting, Mater. Des. 86 (2015) 545–554, https://doi.org/10.1016/j.matdes.2015.07.147.
[6] L. Xiao, W. Song, M. Hu, P. Li, Compressive properties and micro-structural characteristics of Ti–6Al–4V fabricated by electron beam melting and selective laser melting, Mater. Sci. Eng. A 764 (2019), 138204, https://doi.org/10.1016/j.msea.2019.138204.
[7] D. Herzog, V. Seyda, E. Wycisk, C. Emmelmann, Additive manufacturing of metals, Acta Mater. 117 (2016) 371–392, https://doi.org/10.1016/j.actamat.2016.07.019.
[8] S. Bontha, N.W. Klingbeil, P.A. Kobryn, H.L. Fraser, Effects of process variables and size-scale on solidification microstructure in beam-based fabrication of bulky 3D structures, Mater. Sci. Eng. A 513–514 (2009) 311–318, https://doi.org/10.1016/j.msea.2009.02.019.
[9] P. Promoppatum, S.-C. Yao, P.C. Pistorius, A.D. Rollett, A comprehensive comparison of the analytical and numerical prediction of the thermal history and solidification microstructure of Inconel 718 products made by laser powder-bed fusion, Engineering 3 (2017) 685–694, https://doi.org/10.1016/J.ENG.2017.05.023.
[10] O. Gokcekaya, T. Ishimoto, S. Hibino, J. Yasutomi, T. Narushima, T. Nakano, Unique crystallographic texture formation in Inconel 718 by laser powder bed fusion and its effect on mechanical anisotropy, Acta Mater. 212 (2021), 116876, https://doi.org/10.1016/j.actamat.2021.116876.
[11] P. Bidare, I. Bitharas, R.M. Ward, M.M. Attallah, A.J. Moore, Laser powder bed fusion in high-pressure atmospheres, Int. J. Adv. Manuf. Technol. 99 (2018) 543–555, https://doi.org/10.1007/s00170-018-2495-7.
[12] C. Pauzon, P. Forêt, E. Hryha, T. Arunprasad, L. Nyborg, Argon–helium mixtures as laser-powder bed fusion atmospheres: Towards increased build rate of Ti-6Al-4V, J. Mater. Proc. Technol. 279 (2020), 116555, https://doi.org/10.1016/j.jmatprotec.2019.116555.
[13] M. EOS M 290 – Industrial 3D Printed Parts from Metal Materials. ⟨https://www.eos.info/en/additive-manufacturing/3d-printing-metal/eos-metal-systems/eos-m-290⟩. Accessed 21 September 2021.
[14] G.L. Knapp, N. Raghavan, A. Plotkowski, T. DebRoy, Experiments and simulations on solidification microstructure for Inconel 718 in powder bed fusion electron beam additive manufacturing, Addit. Manuf. 25 (2019) 511–521, https://doi.org/10.1016/j.addma.2018.12.001.
[15] H.J. Willy, X. Li, Z. Chen, T.S. Herng, S. Chang, C.Y.A. Ong, C. Li, J. Ding, Model of laser energy absorption adjusted to optical measurements with effective use in finite element simulation of selective laser melting, Mater. Des. 157 (2018) 24–34, https://doi.org/10.1016/j.matdes.2018.07.029.
[16] S. Liu, H. Zhu, G. Peng, J. Yin, X. Zeng, Microstructure prediction of selective laser melting AlSi10Mg using finite element analysis, Mater. Des. 142 (2018) 319–328, https://doi.org/10.1016/j.matdes.2018.01.022.
[17] A. Takase, T. Ishimoto, R. Suganuma, T. Nakano, Lattice distortion in selective laser melting (SLM)-manufactured unstable β-type Ti-15Mo-5Zr-3Al alloy analyzed by high-precision X-ray diffractometry, Scr. Mater. 201 (2021), 113953, https://doi.org/10.1016/j.scriptamat.2021.113953.
[18] Q. Chen, X. Liang, D. Hayduke, J. Liu, L. Cheng, J. Oskin, R. Whitmore, A.C. To, An inherent strain based multiscale modeling framework for simulating part-scale residual deformation for direct metal laser sintering, Addit. Manuf. 28 (2019) 406–418, https://doi.org/10.1016/j.addma.2019.05.021.
[19] T. Ishimoto, K. Hagihara, K. Hisamoto, S.-H. Sun, T. Nakano, Crystallographic texture control of beta-type Ti-15Mo-5Zr-3Al alloy by selective laser melting for the development of novel implants with a biocompatible low Young's modulus, Scr. Mater. 132 (2017) 34–38, https://doi.org/10.1016/j.scriptamat.2016.12.038.
[20] H.S. Carslaw, J.C. Jaeger. Conduction of Heat in Solids, second edition.,, Oxford University Press,, Oxford, 1986.
[21] Y. Li, D. Gu, Parametric analysis of thermal behavior during selective laser melting additive manufacturing of aluminum alloy powder, Mater. Des. 63 (2014) 856–867, https://doi.org/10.1016/j.matdes.2014.07.006.
[22] S.J. Wolff, S. Lin, E.J. Faierson, W.K. Liu, G.J. Wagner, J. Cao, A framework to link localized cooling and properties of directed energy deposition (DED)-processed Ti-6Al-4V, Acta Mater. 132 (2017) 106–117, https://doi.org/10.1016/j.actamat.2017.04.027.
[23] V. Pashkis, A.F.S. Trans 53 (1945) 90.

[24] A. Takase, T. Ishimoto, R. Suganuma, T. Nakano, Surface residual stress and phase stability in unstable β-type Ti-15Mo-5Zr-3Al alloy manufactured by laser and electron beam powder bed fusion technologies, Addit. Manuf. 47 (2021), 102257, https://doi.org/10.1016/j.addma.2021.102257.
[25] R. Rai, P. Burgardt, J.O. Milewski, T.J. Lienert, T. DebRoy, Heat transfer and fluid flow during electron beam welding of 21Cr-6Ni-9Mn steel and Ti-6Al-4V alloy, J. Phys. D: Appl. Phys. 42 (2009), 025503, https://doi.org/10.1088/0022-3727/42/2/025503.
[26] VDI-Gesellschaft Energietechnik, (Engineering Reference Book on Energy and Heat), Springer-Verlag, Berlin Heidelberg,, Heidelberg, 1992.
[27] D.J. Acheson, Elementary Fluid Dynamics, Oxford University Press,, New York, 2005.
[28] D. Agius, K.I. Kourousis, C. Wallbrink, T. Song, Cyclic plasticity and microstructure of as-built SLM Ti-6Al-4V: The effect of build orientation, Mater. Sci. Eng. A 701 (2017) 85–100, https://doi.org/10.1016/j.msea.2017.06.069.
[29] T. Ahmed, H.J. Rack, Phase transformations during cooling in α+β titanium alloys, Mater. Sci. Eng. A 243 (1998) 206–211, https://doi.org/10.1016/S0921-5093(97)00802-2.
[30] Q. Chao, P.D. Hodgson, H. Beladi, Thermal stability of an ultrafine grained Ti-6Al-4V alloy during post-deformation annealing, Mater. Sci. Eng. A 694 (2017) 13–23, https://doi.org/10.1016/j.msea.2017.03.082.
[31] S. Mishra, T. DebRoy, Measurements and Monte Carlo simulation of grain growth in the heat-affected zone of Ti–6Al–4V welds, Acta Mater. 52 (2004) 1183–1192, https://doi.org/10.1016/j.actamat.2003.11.003.
[32] R. Boyer, G. Welsch, E.W. Collings, Materials Properties Handbook. Titanium Alloys, ASM International,, Flevoland, 1994.
[33] J. Yang, H. Yu, J. Yin, M. Gao, Z. Wang, X. Zeng, Formation and control of martensite in Ti-6Al-4V alloy produced by selective laser melting, Mater. Des. 108 (2016) 308–318, https://doi.org/10.1016/j.matdes.2016.06.117.
[34] Y. Chong, T. Bhattacharjee, J. Yi, A. Shibata, N. Tsuji, Mechanical properties of fully martensite microstructure in Ti-6Al-4V alloy transformed from refined beta grains obtained by rapid heat treatment (RHT), Scr. Mater. 138 (2017) 66–70, https://doi.org/10.1016/j.scriptamat.2017.05.038.
[35] T. Ishimoto, K. Hagihara, K. Hisamoto, T. Nakano, Stability of crystallographic texture in laser powder bed fusion: Understanding the competition of crystal growth using a single crystalline seed, Addit. Manuf. 43 (2021), 102004, https://doi.org/10.1016/j.addma.2021.102004.
[36] M. Simonelli, Y.Y. Tse, C. Tuck, On the texture formation of selective laser melted Ti-6Al-4V, Metall. Mater. Trans. A 45 (2014) 2863–2872, https://doi.org/10.1007/s11661-014-2218-0.
[37] P. Wen, L. Jauer, M. Voshage, Y. Chen, R. Poprawe, J.H. Schleifenbaum, Densification behavior of pure Zn metal parts produced by selective laser melting for manufacturing biodegradable implants, J. Mater. Proc. Technol. 258 (2018) 128–137, https://doi.org/10.1016/j.jmatprotec.2018.03.007.
[38] P. Wen, Y. Qin, Y. Chen, M. Voshage, L. Jauer, R. Poprawe, J.H. Schleifenbaum, Laser additive manufacturing of Zn porous scaffolds: Shielding gas flow, surface quality and densification, J. Mater. Sci. Technol. 35 (2019) 368–376, https://doi.org/10.1016/j.jmst.2018.09.065.
[39] D. Wang, S. Wu, F. Fu, S. Mai, Y. Yang, Y. Liu, C. Song, Mechanisms and characteristics of spatter generation in SLM processing and its effect on the properties, Mater. Des. 117 (2017) 121–130, https://doi.org/10.1016/j.matdes.2016.12.060.
[40] H. Amano, Y. Yamaguchi, T. Ishimoto, T. Nakano, Reduction of spatter generation using atmospheric gas in laser powder bed fusion of Ti-6Al-4V, Mater. Trans. 62 (2021) 1225–1230, https://doi.org/10.2320/matertrans.MT-M2021059.
[41] T.F. Broderick, A.G. Jackson, H. Jones, F.H. Froes, The effect of cooling conditions on the microstructure of rapidly solidified Ti-6Al-4V, Metall. Trans. A 16 (1985) 1951–1959, https://doi.org/10.1007/BF02662396.
[42] W. Zhang, Y.M. Jin, A.G. Khachaturyan, Phase field microelasticity modeling of heterogeneous nucleation and growth in martensitic alloys, Acta Mater. 55 (2007) 565–574, https://doi.org/10.1016/j.actamat.2006.08.050.
[43] Y. Liao, C. Ye, B.-J. Kim, S. Suslov, E.A. Stach, G.J. Cheng, Nucleation of highly dense nanoscale precipitates based on warm laser shock peening, J. Appl. Phys. 108 (2010), 063518, https://doi.org/10.1063/1.3481858.
[44] S.-H. Sun, T. Ishimoto, K. Hagihara, Y. Tsutsumi, T. Hanawa, T. Nakano, Excellent mechanical and corrosion properties of austenitic stainless steel with a unique crystallographic lamellar microstructure via selective laser melting, Scr. Mater. 159 (2019) 89–93, https://doi.org/10.1016/j.scriptamat.2018.09.017.
[45] M. Laleh, A.E. Hughes, W. Xu, N. Haghdadi, K. Wang, P. Cizek, I. Gibson, M.Y. Tan, On the unusual intergranular corrosion resistance of 316L stainless steel additively manufactured by selective laser melting, Corros. Sci. 161 (2019), 108189, https://doi.org/10.1016/j.corsci.2019.108189.
[46] T. Ishimoto, R. Ozasa, K. Nakano, M. Weinmann, C. Schnitter, M. Stenzel, A. Matsugaki, T. Nagase, T. Matsuzaka, M. Todai, H.S. Kim, T. Nakano, Development of TiNbTaZrMo bio-high entropy alloy (BioHEA) super-solid solution by selective laser melting, and its improved mechanical property and biocompatibility, Scr. Mater. 194 (2021), 113658, https://doi.org/10.1016/j.scriptamat.2020.113658.
[47] S. Zhonggang, J. Shuwei, G. Yanhua, L. Yichen, C. Lili, X. Fei, Microstructure evolution and mechanical properties of Hastelloy X alloy produced by Selective Laser Melting, High. Temp. Mater. Proc. 39 (2020) 124–135, https://doi.org/10.1515/htmp-2020-0032.
[48] C. Tan, K. Zhou, W. Ma, B. Attard, P. Zhang, T. Kuang, Selective laser melting of high-performance pure tungsten: parameter design, densification behavior and mechanical properties, Sci. Technol. Adv. Mater. 19 (2018) 370–380, https://doi.org/10.1080/14686996.2018.1455154.
[49] A. Das, J.A. Muñiz-Lerma, E.R.L. Espiritu, A. Nommeots-Nomm, K. Waters, M. Brochu, Contribution of cellulosic fibre filter on atmosphere moisture content in laser powder bed fusion additive manufacturing, Sci. Rep. 9 (2019) 13794, https://doi.org/10.1038/s41598-019-50238-5.
[50] C.A. Scholes, U.K. Ghosh, Review of membranes for helium separation and purification, Membranes 7 (2017) 9, https://doi.org/10.3390/membranes7010009.
[51] T.E. Rufford, K.I. Chan, S.H. Huang, E.F. May, A review of conventional and emerging process technologies for the recovery of helium from natural gas, Adsorp. Sci. Technol. 32 (2014) 49–72, https://doi.org/10.1260/0263-6174.32.1.49.